Yiwen Song
Department of Mechanical Engineering,
The Pennsylvania State University,
University Park, PA 16802

James Spencer Lundh
Department of Mechanical Engineering,
The Pennsylvania State University,
University Park, PA 16802

Weijie Wang
Department of Mechanical Engineering,
Texas Center for Superconductivity at UH (TcSUH),
University of Houston,
Houston, TX 77204;
Department of Mechanical Engineering,
Advanced Manufacturing Institute (AMI),
University of Houston,
Houston, TX 77204

Jacob H. Leach
Kyma Technologies, Inc.,
Raleigh, NC 27617

Devon Eichfeld
Department of Mechanical Engineering,
The Pennsylvania State University,
University Park, PA 16802

Anusha Krishnan
Department of Mechanical Engineering,
The Pennsylvania State University,
University Park, PA 16802

Carlos Perez
Department of Mechanical Engineering,
The Pennsylvania State University,
University Park, PA 16802

Dong Ji
Department of Electrical Engineering,
Stanford University,
Stanford, CA 94305

Trent Borman
Department of Materials Science and Engineering,
The Pennsylvania State University,
University Park, PA 16802

Kevin Ferri
Department of Materials Science and Engineering,
The Pennsylvania State University,
University Park, PA 16802

Jon-Paul Maria
Department of Materials Science and Engineering,
The Pennsylvania State University,
University Park, PA 16802

The Doping Dependence of the Thermal Conductivity of Bulk Gallium Nitride Substrates

Gallium nitride (GaN) has emerged as one of the most attractive base materials for next-generation high-power and high-frequency electronic devices. Recent efforts have focused on realizing vertical power device structures such as in situ oxide, GaN interlayer based vertical trench metal–oxide–semiconductor field-effect transistors (OG-FETs). Unfortunately, the higher-power density of GaN electronics inevitably leads to considerable device self-heating which impacts device performance and reliability. Halide vapor-phase epitaxy (HVPE) is currently the most common approach for manufacturing commercial GaN substrates used to build vertical GaN transistors. Vertical device structures consist of GaN layers of diverse doping levels. Hence, it is of crucial importance to measure and understand how the dopant type (Si, Fe, and Mg), doping level, and crystal quality alter the thermal conductivity of HVPE-grown bulk GaN. In this work, a steady-state thermoreflectance (SSTR) technique was used to measure the thermal conductivity of HVPE-grown GaN substrates employing different doping schemes and levels. Structural and electrical characterization methods including X-ray diffraction (XRD), secondary-ion mass spectrometry (SIMS), Raman spectroscopy, and Hall-effect measurements were used to determine and compare the GaN crystal quality, dislocation density, doping level, and carrier concentration. Using this comprehensive suite of characterization methods, the interrelation among structural/electrical parameters and the thermal conductivity of bulk GaN substrates was investigated. While doping is evidenced to reduce the GaN thermal conductivity, the highest thermal conductivity (201 W/mK) is observed in a heavily Si-doped ($1–5.00 \times 10^{18}$ cm^{-3}) substrate with the highest crystalline quality. This suggests that phonon-dislocation scattering dominates over phonon-impurity scattering in the tested HVPE-grown bulk GaN substrates. The results provide useful information for designing thermal management solutions for vertical GaN power electronic devices. [DOI: 10.1115/1.4047578]

Keywords: gallium nitride (GaN), power electronics, Raman spectroscopy, steady-state thermoreflectance, vertical power devices, wide bandgap semiconductors

[1]Corresponding author.

Contributed by the Electronic and Photonic Packaging Division of ASME for publication in the Journal of Electronic Packaging. Manuscript received January 13, 2020; final manuscript received June 2, 2020; published online July 10, 2020. Assoc. Editor: Sreekant Narumanchi.

Srabanti Chowdhury
Department of Electrical Engineering,
Stanford University,
Stanford, CA 94305

Jae-Hyun Ryou
Department of Mechanical Engineering,
Texas Center for Superconductivity at UH
(TcSUH)
University of Houston,
Houston, TX 77204;
Department of Mechanical Engineering,
Advanced Manufacturing Institute (AMI),
University of Houston,
Houston, TX 77204

Brian M. Foley
Department of Mechanical Engineering,
The Pennsylvania State University,
University Park, PA 16802

Sukwon Choi[1]
Department of Mechanical Engineering,
The Pennsylvania State University,
University Park, PA 16802
e-mail: sukwon.choi@psu.edu

1 Introduction

Gallium nitride (GaN) has been extensively studied as the base material for next-generation power electronics due to its large critical electric field ($E_{cr} \sim 3.3$ MV/cm) resulting from its wide bandgap ($E_g = 3.4$ eV), and high electron saturation velocity ($V_s = 3 \times 10^7$ cm/s) [1]. Replacement of conventional Si devices to GaN-based power electronics is being sought for in order to achieve system-level benefits such as reduced form factor, higher operating power, and improved energy conversion efficiency. Commercial lateral AlGaN/GaN high electron mobility transistors (HEMTs) are available which operate at $V_{DS} = 600$ V and $I_{DS} = 10$ A. The low device ON-resistance is achieved due to the formation of a two-dimensional electron gas (2-DEG) which serves as the current channel. However, dynamic on-resistance and current collapse are limiting device performance for lateral structures [2,3]. Furthermore, due to the geometric restriction of the 2-DEG formation, the distance between drain and source must be increased to avoid large electric fields for high-power applications, resulting in larger chip size [4]. As a result, GaN HEMTs are often used for medium power applications to operate at a power level less than 10 kW [5,6]. For high-power (100 kW) applications such as large-scale power conversion, a vertical geometry for GaN transistors is preferred due to better area-efficiency and power handling capability [5]. Ji et al. have reported a breakdown voltage of 900 V and an on-resistance of 4.1Ω for an metal–oxide–semiconductor field-effect transistors (OG-FET) [7]. Reducing the size and weight of the power conversion unit is desired for numerous applications in aerospace, automobile, and medical engineering [8]. For example, a compact and efficient power conversion unit for electric vehicle leaves more passenger space for comfort and improves miles per gallon of gasoline-equivalent (MPGe) for longer travel range.

While vertical GaN transistors enhance the area efficiency and enable higher operating power, the increased power density also raises potential concerns for severe thermal issues. Self-heating is known to degrade device electric performance and to reduce component lifetime; moreover, the induced thermal stress could also compromise system mechanical stability [9]. Extensive thermal characterization on GaN thin films has been done, relevant to lateral GaN device structures, for thermal management purposes; however, construction of a vertical GaN device involves a more complex stack of bulk GaN whose thermal properties are not well understood. For example, the OG-FET layer stack includes a free-standing n^+-GaN substrate, a lightly doped n-GaN epitaxial layer, a heavily doped p^+-GaN, and a heavily doped n^+ GaN as shown in Fig. 1 [5,6]. The complexity of the different doping levels raises challenges to accurate device thermal modeling.

The thermal conductivity of bulk single crystal GaN was reported to be as high as 230 W/mK [10]; however, doping is known to impact lattice thermal conductivity due to additional phonon-scattering mechanisms associated with impurity atoms [11]. Employing a single thermal conductivity value (e.g., 230 W/mK) for thermal modeling of an OG-FET without taking consideration of the doping dependence of the thermal conductivity can lead to a significant underestimation of device self-heating. This, in turn, may lead to significantly overpredicted device lifetimes where this false prediction may lead to catastrophic events in reliability critical applications [12–16].

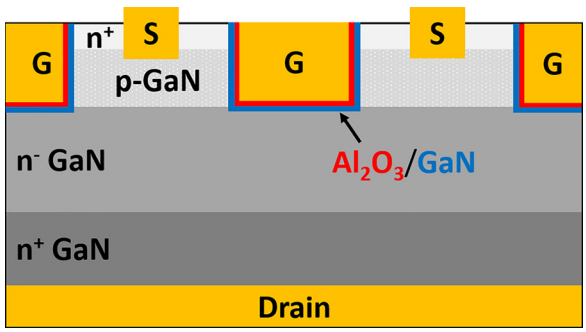

Fig. 1 Schematic cross section of an OG-FET

Halide vapor-phase epitaxy (HVPE) is currently the most common approach for manufacturing commercial GaN substrates used to build lateral and vertical GaN transistors [17,18]. Previous studies [19] on the doping dependence of the GaN thermal conductivity were focused on 1–4 μm thick GaN layers grown via metal-organic chemical vapor deposition (MOCVD) [20] or molecular beam epitaxy (MBE) [21]. However, GaN materials synthesized via different methods exhibit different levels of impurities, dislocation densities, unintentional doping, and deep-level defect concentrations [22]. These defects directly impact electronic [22–24] and thermal [10,22,25–30] transport. Thermal transport in GaN is also affected by the layer thickness variation which is revealed by the strong thickness dependence of the GaN thermal conductivity [19,31,32]. Table 1 summarizes the reported GaN thermal conductivity values for materials with different thicknesses and growth methods. The thickness dependence is apparent for GaN thin films where the layer thickness is comparable to the effective mean-free path of phonons. At room temperature, more than 50% of heat conduction in the GaN is carried by phonons with mean free paths greater than 400 nm [33]; therefore, when the layer thickness is orders of magnitude higher than this effective mean free path, the thermal conductivity approaches a bulk value and becomes insensitive to thickness. Reference [34] has shown a minimal change in the room temperature thermal conductivity of GaN materials with thicknesses spanning 5 μm to 500 μm. Although extensive studies have characterized the thermal conductivity of GaN thin films and substrates, the knowledge of the doping dependence (i.e., dopant atoms and doping levels) on the thermal conductivity of HVPE-grown bulk GaN is limited.

In this work, multiple Si-, Fe-, and Mg-doped (at different doping levels) HVPE bulk GaN substrates were characterized using a steady-state thermoreflectance (SSTR) technique [38]. SSTR is an optical pump-probe technique best suited for thermal property measurement for bulk materials as compared to frequency- and time-domain thermoreflectance methods [39,40], that have been used for characterization of GaN thin films; the experimental setup is discussed in detail in this paper. While the experimental results reveal the reduction of GaN thermal conductivity by introducing substitutional atoms (dopants), among the tested samples, the highest thermal conductivity (201 W/mK) was observed in an n^+ bulk GaN substrate with highest crystalline quality despite being heavily doped with Si. The results provide key insight into the effective thermal management of vertical GaN power devices that include heavily doped regions.

2 Sample Preparation and Experimental Methods

Hydride vapor-phase epitaxy (HVPE)-grown GaN samples were prepared with different doping schemes and concentrations. SSTR was used to measure the thermal conductivity of the samples. The free carrier concentration of the samples was characterized by Hall-effect measurement and confirmed by Raman spectroscopy. Impurity concentration was measured by secondary-ion mass spectrometry (SIMS). Edge and screw dislocation densities were quantified by high-resolution X-ray diffraction (XRD), and the crystal quality was confirmed by Raman spectroscopy measurements.

2.1 Halide Vapor-Phase Epitaxy-GaN Substrates. Halide vapor-phase epitaxy is a well-established method for growing a number of compound semiconductor materials and is the dominant technique used today to produce free-standing n^+ and semi-insulating (using compensation doping) GaN substrates. The technique relies on the reaction of NH_3 with GaCl (which is produced upstream of the growth via a reaction between HCl or Cl_2 with high-purity Ga metal at ~850 °C) to produce GaN at temperatures of ~1050 °C. The ability to achieve growth rates as high as 300 μm per hour during GaN growth is key to its use in GaN substrate technology. Additionally, compared to MOCVD which relies on carbon-containing metalorganics as Ga precursors, HVPE is a carbon-free growth process, but the incorporation of Si and/or O impurities at concentrations of $\sim 1 \times 10^{17}\,\mathrm{cm}^{-3}$ is common due to the quartz environment of the reactor and results in n-type crystals [18,41,42]. Despite this, GaN layers can be made to be purer, as evidenced by recent demonstrations by Kyma and others in which GaN films with low background electron concentrations ($2 \times 10^{14}\,\mathrm{cm}^{-3}$) were realized [41]. Five GaN Samples were grown via HVPE in this study:

(1) The unintentional doped (UID) GaN has a thickness of 260 μm and slightly n-type due to the background Si impurities that are present in quartz-based HVPE growth of GaN. The substrate resistivity is 0.0692 Ω-cm.
(2) The semi-insulating (SI) GaN has a thickness of 505 μm and is counter doped with Fe. The substrate resistivity is larger than 10^6 Ω-cm.
(3) The p-type (p) GaN has a thickness of 500 μm and is Mg-doped. The substrate resistivity was measured to be 424 Ω-cm.
(4) The n-type (n) GaN substrate is Si-doped and has a thickness of 493 μm. The resistivity of the n^+ sample is 0.0217 Ω-cm.
(5) The heavily n-doped (n^+) GaN substrate is also Si-doped and is 400 μm thick.

2.2 Steady-State Thermoreflectance. The SSTR method is an optical pump-probe technique suitable for extracting the thermal conductivity of bulk materials [38]. A pump laser is modulated with a square wave to induce a periodic heat flux (ΔP); the modulation frequency is low enough that the internal temperature profile of the material reaches steady-state under heating/cooling conditions. Due to the periodic change in temperature, ΔT, a change in transducer reflectivity is induced; the difference between the "cold" and "hot" reflectivity values is denoted by ΔR. The reflectivity change is measured by the reflected probe laser intensity with a balanced photodetector; a lock-in detection scheme is required to capture the small change in the thermoreflectance signal. The balanced photodetector signal is denoted as $\Delta V/V$, where V is the reference reflected probe intensity for the "cold" state and ΔV is the change in the reflected probe intensity between the "cold" and "hot" states. A schematic of the process is shown in Fig. 2.

The transducer reflectivity ΔR is linearly proportional to the change in temperature ΔT. Since the temperature is also a linear

Table 1 Reported values for GaN thermal conductivity

	Thickness (μm)	Thermal conductivity (W/mK)	Growth method	Reference
Film	3–4	110–180	MOCVD	[19]
	0.9/1.3	167/185	MOCVD/MBE	[35]
	0.015–1	0–120	MBE	[31]
	0.064	150	MBE	[36]
	5	155	MOCVD	[37]
Bulk	N/A	195–230	HVPE	[10]
	N/A	164–196	Ammonothermal	[34]

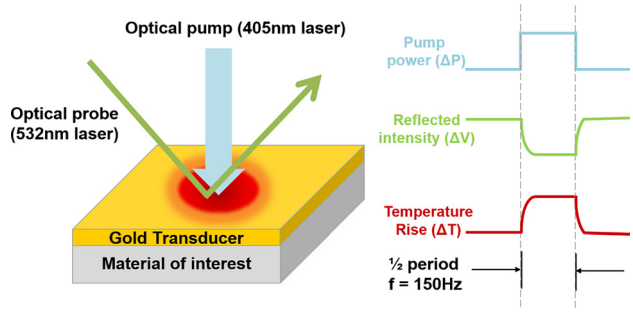

Fig. 2 Operating principle of SSTR. The pump and probe are aligned co-axially in the actual setup. The reflectance of gold at 532 nm decreases with increasing temperature; therefore, ΔV drops at the higher temperature.

function of heat flux as a result of steady-state heating, the aforementioned variables can be related by

$$\frac{\Delta V}{V} \propto \frac{\Delta R}{R} \propto \Delta T \propto \Delta P \tag{1}$$

By re-arranging terms in Eq. (1)

$$\frac{\Delta V}{V \Delta P} = \gamma \left(\frac{\Delta T(\kappa)}{\Delta |Q|} \right) \tag{2}$$

where $\Delta|Q|$ is the heat flux used in the model, $\Delta T(\kappa)$ is the modeled temperature rise as a function of material thermal conductivity κ, and γ is a correction factor. The left side of the Eq. (2) is obtained by performing linear regression on the experimentally obtained $\Delta V/V$ and ΔP data. A given heat flux would induce a larger temperature rise for low-thermal conductivity materials; for example, sapphire ($\kappa = 33$ W/mK) has a steeper slope on a $\Delta V/V$ versus ΔP plot than silicon ($\kappa = 135$ W/mK) does, as shown in Fig. 3. γ can be found by relating this slope to a thermal model based on Fourier's law. A detailed discussion about this analytical model can be found in Ref. [43]. By depositing the same transducer on a calibration sample with a well-known thermal conductivity (e.g., silicon and/or sapphire), the γ value can be extracted

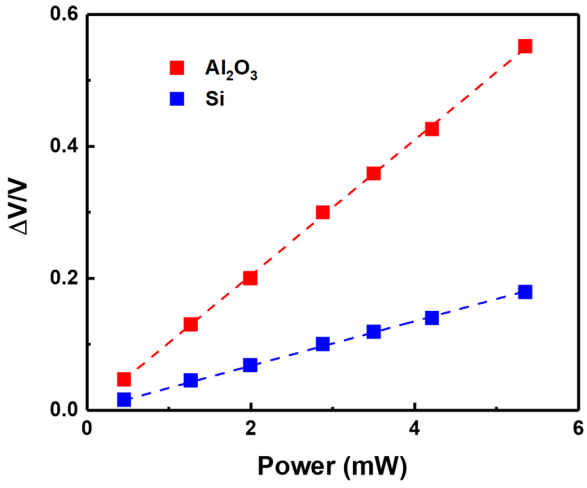

Fig. 3 A comparison of SSTR signals for sapphire and silicon. Since silicon has a higher thermal conductivity ($\kappa = 135$ W/mK) than sapphire ($\kappa = 33$ W/mK), it has a smaller temperature rise for a given pump laser power and therefore a smaller change in reflectance.

and used to fit the thermal conductivity of the materials to be analyzed.

For the setup used in this study, the pump and probe were continuous wave solid-state lasers. The pump (COHERENT OBIS 405 nm LX 200 mW, Santa Clara, CA) has a wavelength of 405 nm and a power rating of 200 mW. The probe (COHERENT OBIS 532 nm LS 100 mW, Santa Clara, CA) has a wavelength of 532 nm and a power rating of 100 mW. During experiments, maximum output powers were used for both lasers to ensure the best laser power stability; waveplates and neutral-density (ND) filters are used to adjust the laser power incident on the samples. The pump laser was modulated at 150 Hz with a mechanical chopper (Thorlabs MC20000B, Newton, NJ). The pump intensity ΔP was measured by a photodetector (Thorlabs DET10A2) paired with a 92:8 (92% transmission/8% reflection) beam splitter. The pump and probe lasers were focused on the sample with a 5× objective (Olympus MPlan N 5×/0.10). A long-pass dichroic mirror (Thorlabs DMLP505) on a kinematic mount (Thorlabs KM100CP) was used to precisely align the pump and probe beam spots on the sample surface; the best alignment is achieved when a maximum value of ΔV is detected. A balanced photodetector (Thorlabs PDB425A—AC) was used to pick up the reference probe signal, V, and the reflected probe signal, ΔV; the photodetector signals were monitored with a lock-in amplifier (Zurich Instruments HF2 LI, Zurich, Switzerland). During experiments, a motorized filter wheel (Thorlabs FW212CNEB) loaded with ND filters at different levels was used to sweep pump laser power, and the corresponding ΔP, ΔV, and V were recorded with an oscilloscope for postprocessing. The pump and probe radius were measured using a scanning-slit optical beam profiler (Thorlabs BP209-VIS) to evaluate the probe-averaged temperature rise used in the thermal analytical model [38,43]. A schematic of the setup is shown in Fig. 4.

With the thickness of all the GaN samples well above the thermal penetration depth of the pump laser heating (~8 μm), a two-layer semi-infinite model was used in the Fourier-model to calculate the temperature rise. Silicon and sapphire were used as calibration samples to find the proportionality constant γ, and they showed excellent agreement. All of the HVPE-GaN samples were deposited with 80 nm Au transducer layers via sputtering to enable SSTR measurements. In order to minimize the uncertainty in the analysis of the SSTR data, transducer thicknesses were measured via X-ray reflectometry.

2.3 High-Resolution X-Ray Diffraction. High-resolution XRD was used to assess the crystal orientation and quality of the GaN samples. A Bruker D8 discover high-resolution X-ray diffractometer with a Ge (022)×4 monochromator was used as the first optics and pathfinder variable slit multiple beam analyzer was used as the secondary optics. A 2θ–ω scan was performed to characterize the out-of-plane orientation of the GaN substrates as shown in Fig. 5(*a*). The main peaks with significant intensity were found to be GaN (002) and GaN (004) diffraction patterns, which confirm the c-axis orientation. The other low-intensity peaks come from the diffraction of the background sample holder.

The XRD φ scan for asymmetric planes of (105) in GaN is shown in Fig. 5(*b*). The six separate peaks with 60 deg interval represent the six fold rotational symmetry of the wurtzite structure and confirm that GaN was grown as a single crystalline material.

The XRD rocking curves for a set of quasi-symmetric (skew geometry) planes with different inclination angles were measured to estimate the threading dislocation density of different GaN samples. The impact of the screw and edge threading dislocations on the width of the X-ray reflections in the limiting cases of lattice planes parallel and perpendicular to the surface is commonly referred to as tilt and twist, respectively [44]. The tilt describes the rotation of the mosaic blocks out of the growth plane, and the twist of their in-plane rotation. The tilt of (001)-oriented GaN layers can be correlated to the density of screw threading dislocations with Burgers vector $\mathbf{b} = [0001]$, and usually expressed as the

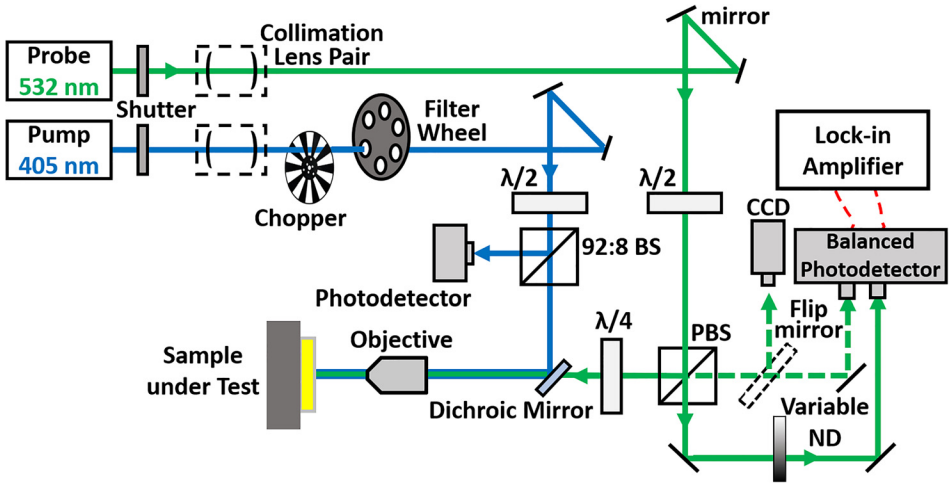

Fig. 4 Schematic of the SSTR setup. The probe laser (532 nm) travels through a collimation lens pair and a half waveplate ($\lambda/2$) and is split into two paths with a polarized beam splitter. One path passes through the quarter waveplate ($\lambda/4$) and dichroic mirror, and it is focused on the sample; the other path passes through a variable neutral density filter (variable ND) and focuses on the photodetector. The pump laser (405 nm) travels through a collimation lens pair and a half waveplate ($\lambda/2$), and it is split into two paths with a 92% transmission/8% reflection beam splitter (92:8 beam splitter). The 92% transmitted path is reflected by a dichroic mirror to align with the probe spot on the sample, and the 8% reflected path is collected by a photodetector as the ΔP signal. The reflected probe laser (dashed line) passes through the polarized beam splitter and focuses on the photodetector. A flip mirror and a CCD camera are used to check proper focus on the sample surface.

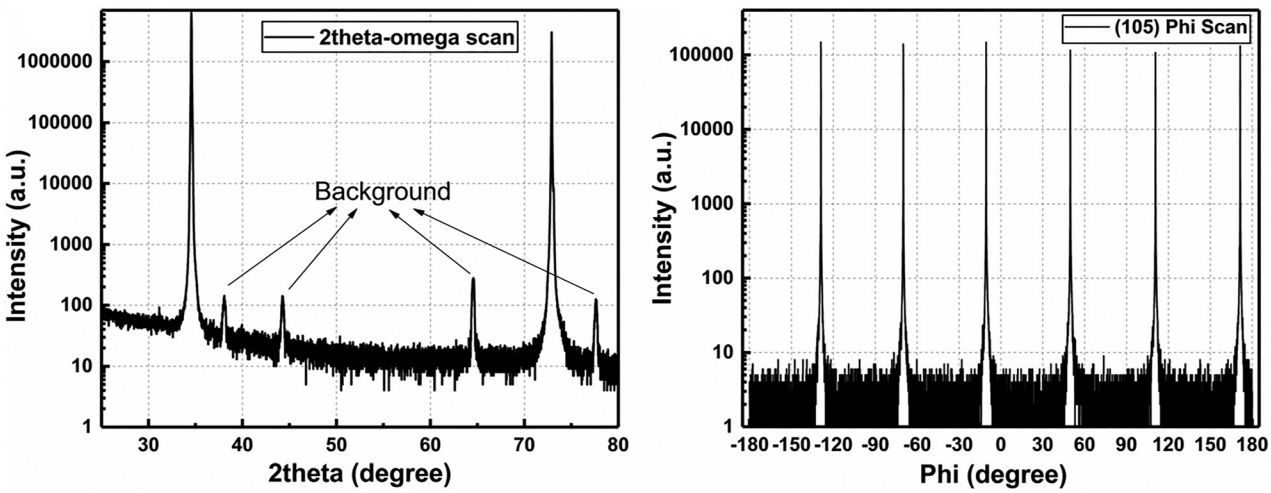

(*a*) (*b*)

Fig. 5 (*a*) 2θ–ω scan and (*b*) ϕ scan for asymmetric planes of (105)

full width half maximum (FWHM) of the surface normal (001) X-ray rocking curves ($\Delta\omega_s$). The twist is connected to the density of edge threading dislocations with $b = (1/3) < 11\bar{2}0 >$ and expressed as FWHM of in plane (100) rocking curves ($\Delta\omega_e$) [45]. The equations for dislocation density calculation are shown below [46,47]:

$$\rho_e = \frac{\Delta\omega_e^2}{4.35\mathbf{b}_e^2} \tag{3}$$

$$\rho_s = \frac{\Delta\omega_s^2}{4.35\mathbf{b}_s^2} \tag{4}$$

with the coefficient $2\pi ln2 \approx 4.35$, $\mathrm{b}_e = 0.3189$ nm, and $\mathbf{b}_s = 0.5189$ nm.

As shown in Fig. 6(*a*), the X-ray rocking curves of skew symmetric planes were measured and FWHM of these planes are plotted versus inclination angle. Asymmetry and side peaks are observed in these planes as shown in Fig. 6(*b*), and multiple peak fitting was applied to separate the side peaks and obtain the FWHM value for each plane. Unlike most GaN films on silicon or sapphire grown by MOCVD, Fig. 6(*a*) does not show a monotonic increase in FWHM with an increasing inclination angle [48]. Instead, the FWHM increases first and then decreases. This can be originated from the different preferred tilting angles from (002) rocking curves as shown in Fig. 6(*b*). As the inclination angle increase, the separate peaks start to overlap, resulting in peak broadening and increment of (105) (103) (102) FWHM, and then separates away, resulting in the decrement of FWHM. Planes with a higher inclination angle are less affected by these separate tilting domains and thus results in the decrement of FWHM after (102) plane.

Among several reported methods to determine the twist [46,49,50], the most common procedure is by extrapolating the

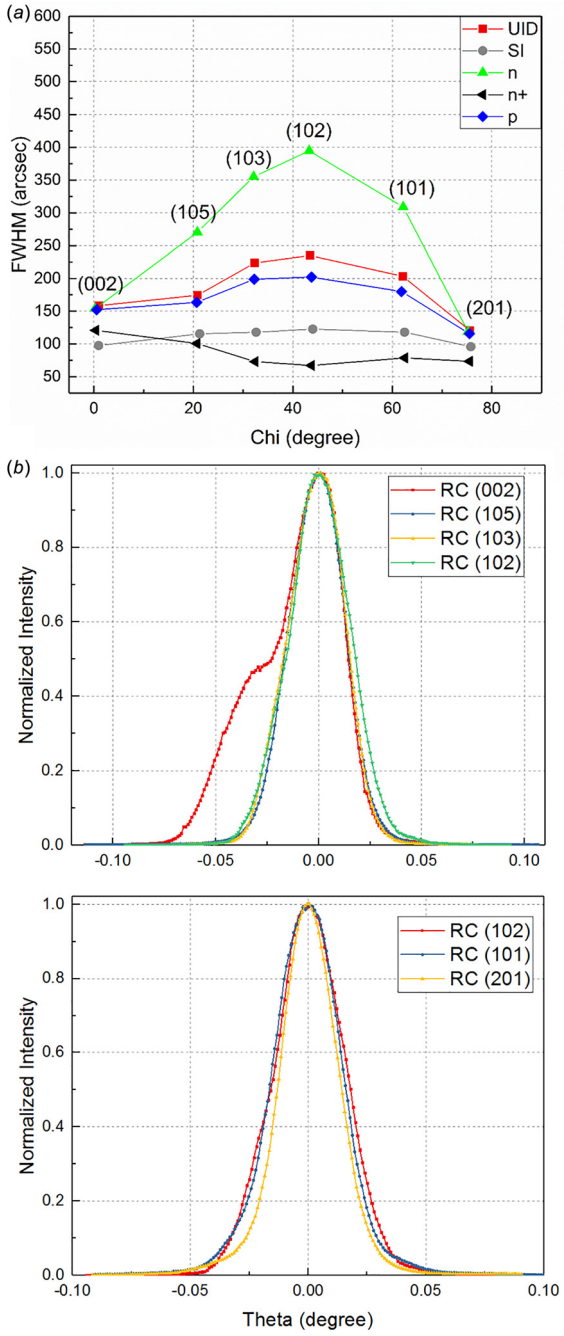

Fig. 6 (*a*) FWHM of skew symmetric planes versus inclination angle and (*b*) preferred tilting angles from (002) rocking curves

FWHM data to $\varphi = 90$ deg [49]. However, our results did not show a monotonic trend and affected by the peak separation due to different preferred tilting domains. Thus, the (201) rocking curve with a high-inclination angle of 76 deg is used to estimate the twist.

2.4 Van Der Pauw Hall Measurement. Van der Pauw Hall measurements were performed using an Ecopia HMS-3000 Hall system. Ohmic contacts were fabricated by Ti/Al/Ni/Au metal stacks followed by 850 °C annealing in a nitrogen ambient for *n*-type GaN samples and Ni/Au metal stacks followed by 450 °C annealing in oxygen for the *p*-type GaN sample. Room temperature Hall measurement results are shown in Table 2.

The AC and BD Hall coefficients show good consistency along the two diagonal directions for the square samples. However, a current spreading effect was observed in the *p*-type and SI samples due to their irregular shapes and resulted in variation of AC and BD cross Hall coefficients.

2.5 Raman Spectroscopy. Raman spectroscopy was performed using a Horiba LabRAM HR evolution spectrometer equipped with an 1800 grooves/mm grating and 532 nm excitation. Since the energy of the laser excitation (~2.33 eV) was less than the bandgap energy of GaN (~3.4 eV), all samples were transparent to the incident radiation and laser heating was assumed to be negligible; therefore, a laser power of 1 mW was used to maximize the signal-to-noise ratio. A 50× long working distance objective (numerical aperture = 0.45) was used to probe the GaN samples, offering a spatial resolution of ~1 μm and a probing depth of ~10 μm [51].

Raman spectroscopy is an experimental method that is generally applied for material characterization, temperature measurements, and stress analysis [52–54]; however, it can also be applied for qualitative electrical characterization. The A_1(LO) phonon mode of GaN is a phonon–plasmon coupled mode that can qualitatively assess the free carrier concentration in GaN samples. As the free carrier concentration in GaN increases, the phonon–plasmon coupling of the A_1(LO) phonon mode results in a decrease in the intensity of the A_1(LO) Raman peak, while the linewidth and frequency of the A_1(LO) Raman peak increase [55]. This behavior is shown in Fig. 7 for the GaN samples tested in this study and shows good agreement with the Hall measurements reported in Table 2.

To assess the crystalline quality of the GaN samples, the linewidth of the characteristic GaN Raman peaks can be analyzed. According to Heisenberg's uncertainty principle, as the crystalline quality increases, the linewidth of the phonon mode will decrease because of the phonon lifetime increases [56]. However, since the linewidth of the A_1(LO) phonon mode is also sensitive to free carrier concentration, the linewidth of the GaN E_2(high) phonon mode from the Raman spectra was analyzed. For example, although the n^+ sample has the highest free carrier concentration, the linewidth of the E_2(high) mode for this sample was the narrowest, suggesting this sample has the greatest crystalline quality as shown in Fig. 8(*b*). Details regarding probing of the GaN crystallinity using micro-Raman spectroscopy were presented in Sec. 3.

2.6 Secondary Ion Mass Spectrometry. Secondary ion mass spectrometry measurements were performed using a commercial vendor (Evans Analytical Group). Metals (Fe, Mg), were analyzed using a duoplasmatron source with O_2^+ ions with an impact energy of 5.5 keV. Nonmetals (H, C, O, and Si) were analyzed using a Cs ionizer source with Cs^+ ions using an impact energy of 14.5 keV

Table 2 Room temperature Hall measurement results

	Bulk con.	Mobility (cm^2/V_s)	Thickness (μm)	AC Hall (cm^3/C)	BD Hall (cm^3/C)	Shape
p	1.125×10^{16}	69.4	500	169.5	858.1	Stripe
SI	N/A	42.2	505	–234.5	–243.9	Triangular
UID	-8.977×10^{17}	330	260	−6.956	−6.952	Square
N	-1.185×10^{18}	411	493	−5.259	−5.274	Square
n^+	-3.446×10^{18}	307	400	−1.859	−1.764	Near square

The free carrier concentration of the SI sample was below the detection limit of Hall measurement.

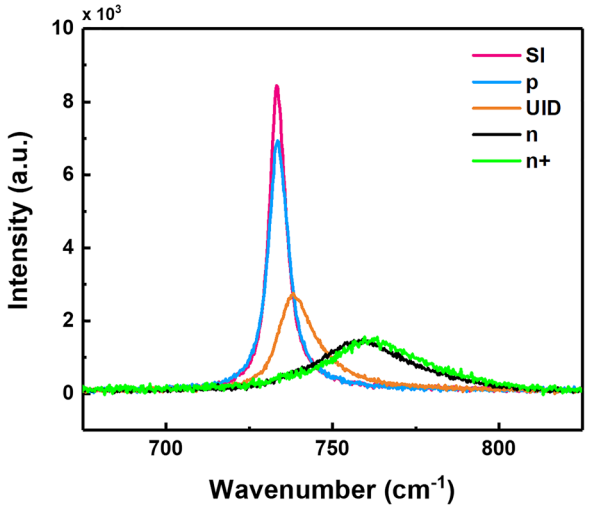

Fig. 7 A_1(LO) Raman peak the measured samples. The blue shift, line broadening, and intensity drop show an increasing carrier concentration from SI, *p*-type, UID, *n*-type, to n^+ sample.

for bulk analyses of the SI and *p*-type samples or 4 keV for profile analyses of the UID, *n*-type, and n^+ samples. The same reference standards were used for both types of analyses, making the results comparable among all samples analyzed in this study.

3 Results and Discussion

Doping is commonly used to tailor the electronic characteristics of semiconductor materials to fabricate functional devices. By adding dopants into the material, electron- or hole-concentrations are changed, resulting in *n*-type or *p*-type materials, respectively. Precise control of the free carrier (electrons or holes) concentration is essential to fabricate electronic devices. Figure 9 shows the free carrier concentration of each GaN substrate obtained from Van der Pauw Hall measurements. Observation of the A_1(LO) Raman peak also provides qualitative means for determining the free carrier concentration in GaN [55,57,58]. The strong coupling between the A_1(LO) phonon mode and the free carriers (plasmons) result in a blue shift of the A_1(LO) phonon peak to higher frequencies, broadening of the line shape, and reduction of the peak intensity. An excellent correlation between the Raman and Hall measurements is evidenced in Figs. 7 and 9 where, for example, the n^+ sample has a significantly lower peak intensity, a broader linewidth, and a peak location at a higher wavenumber as compared to the SI sample. The measured thermal conductivity of GaN films (via SSTR) and the free carrier concentration of the GaN samples are listed in Table 3. The uncertainty was calculated based on measurements performed on six different locations of each sample.

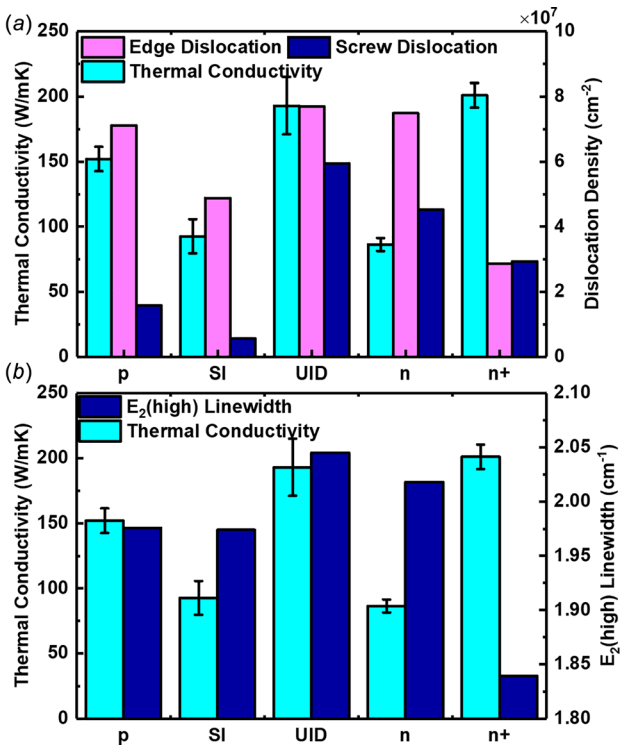

Fig. 8 (*a*) Dislocation density measured by XRD versus thermal conductivity and (*b*) Raman E_2 (high) line width versus thermal conductivity. A narrower E_2 (high) linewidth indicates an overall better crystallinity.

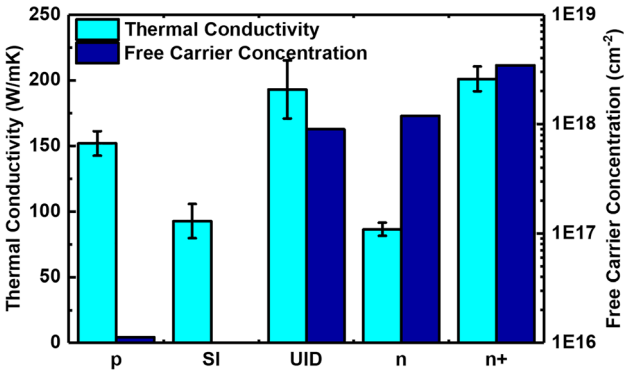

Fig. 9 Thermal conductivity versus free carrier concentration of the GaN substrates. The free carrier concentrations for all samples are shown absolute values for a better comparison between *p*-type and *n*-type materials. The free carrier concentration for the SI sample is below the detection limit as expected.

The relationship between thermal conductivity and the measured free carrier concentration of the GaN samples is plotted in Fig. 9. Thermal conductivity does not show an apparent correlation with free carrier concentration. The reason is that the electronic contribution to the thermal conductivity is negligible for carrier (electrons and/or holes) concentrations less than 10^{19} cm^{-3} [59]. It should be noted that the highest electron concentration among the tested samples was 3.45×10^{18}. Therefore, the subsequent analysis focuses on phonon-scattering processes that limit thermal transport within the GaN crystal.

A phonon is a quantum of vibrational mechanical energy in a crystal lattice. Acoustic phonons and optical phonons govern the macroscopically observable thermal properties of crystalline materials. Phonons are central thermal energy carriers that drive heat conduction in nondegenerate semiconductors and insulators. According to the kinetic theory, a simplified expression for the lattice thermal conductivity, κ is

$$\kappa = \frac{1}{3}\sum_{p} c(T)v(T)\Lambda(T) \tag{5}$$

where p denotes particular phonon branches, T is the temperature, $c(T)$ is the lattice specific heat, $v(T)$ is the phonon group velocity, and $\Lambda(T)$ is the effective mean-free path of phonons that contribute to heat conduction (primarily acoustic modes).

The phonon mean-free path $\Lambda(T)$ in Eq. (5) is governed by various phonon-scattering events ($\Lambda = v\tau_{\text{eff}}$). The effective scattering time (τ_{eff}) can be calculated via Matthiessen's rule

$$\frac{1}{\tau_{\text{eff}}} = \frac{1}{\tau_i} + \frac{1}{\tau_d} + \frac{1}{\tau_u} \tag{6}$$

Table 3 Summary of measured thermal conductivity, free carrier concentration, and dislocation density

	p	SI	UID	n	n^+
Dopant	Mg	Fe	Si	Si	Si
Thermal conductivity (W/mK)	152 ± 9.4	92.7 ± 13	193 ± 22	86.5 ± 5.0	201 ± 9.4
Free carrier concentration (cm^{-2})	1.13×10^{16}	N/A	-8.98×10^{17}	-1.19×10^{18}	-3.45×10^{18}
Thickness (μm)	500	505	260	493	400
Screw dislocation (cm^{-2})	1.59×10^7	5.65×10^6	5.95×10^7	4.52×10^7	2.94×10^7
Edge dislocation (cm^{-2})	7.11×10^7	4.88×10^7	7.70×10^7	7.49×10^7	2.87×10^7

For the Fe-doped SI substrate, the carrier concentration was below the reliable detection limit of the Hall measurement.

Table 4 SIMS measurement results

	O	H	C	Si	Fe	Mg
P	$<2.00 \times 10^{16}$	N/A	$<1.00 \times 10^{16}$	$1–2.00 \times 10^{16}$	N/A	3.00×10^{18}
SI	3.00×10^{16}	N/A	7.00×10^{16}	1.00×10^{16}	5.00×10^{17}	N/A
UID	2.00×10^{16}	1.00×10^{18}	$<5.00 \times 10^{15}$	1.00×10^{16}	N/A	N/A
n	2.00×10^{16}	1.00×10^{18}	$<5.00 \times 10^{15}$	2.00×10^{18}	N/A	N/A
n^+	1.00×10^{17}	2.00×10^{17}	1.00×10^{17}	$1–5.00 \times 10^{18}$	N/A	N/A

where τ_u is the scattering time associated with Umklapp processes, and τ_i and τ_d are impurity and dislocation scattering times, respectively. In general, an overall longer scattering time (τ_{eff}) results in a longer effective phonon mean free path $\Lambda(T)$ and thus higher lattice thermal conductivity.

During HVPE growth, silicon and oxygen atoms are often unintentionally introduced into the resulting GaN crystal due to precursors attacking quartz reactor tubes [18,41,42]; therefore, UID GaN is natively n-type, and additional dopants are added to achieve the desired electronic transport characteristics. For the n-type samples (n and n^+), silicon (Si) was added to achieve higher free carrier concentration. The SI sample was counterdoped with iron (Fe) to obtain a semi-insulating material. The p-type sample was magnesium (Mg) doped. Impurity concentrations for each sample were measured via SIMS and results are summarized in Table 4. It should be noted that the activation for Mg-doped GaN is difficult due to the presence of deep hole trap levels [60,61]; therefore, the free carrier concentration determined by Hall measurement is orders of magnitude lower than the Mg-atom concentration measured by SIMS. The addition of foreign atoms, i.e., dopants, increases the phonon-impurity scattering rate (τ_i^{-1}), or the reciprocal of the phonon-impurity scattering time (τ_i), which reduces the thermal conductivity.

Due to the simultaneous influence of free carriers, impurities, and crystallinity on thermal conductivity, subsequent analysis of the crystal quality of the samples was performed. Screw and edge dislocations of each sample were measured via high-resolution XRD. It should be noted that XRD measurement for bulk GaN samples is challenging because of the peak separation with different preferred tilting domains. Therefore, the E_2(high) phonon linewidth (FWHM) of the GaN substrates were also measured using Raman spectroscopy in order to qualitatively compare the crystalline quality of each sample. The dislocation densities and Raman linewidths are plotted versus thermal conductivity in Figs. 8(*a*) and 8(*b*).

With a similar crystallinity indicated by Raman linewidths, the reduction of thermal conductivity due to the phonon-impurity scattering is evidenced by the lower-thermal conductivity of the p-type, SI, and n-type GaN substrates as compared to the UID GaN sample, as shown in Figs. 8(*b*) and 8(*a*). The size and weight of the dopant atoms both affect the impurity scattering; with a similar dopant concentration, the higher thermal conductivity of the p-type GaN as compared to that of the n-type GaN can be explained by the smaller degree of lattice distortion by Mg substitution (as compared to Si) for the Ga cation-sites [62–64]. However, for the n^+ GaN sample, although more Si dopants were incorporated into the GaN crystal to achieve higher free carrier concentration, it showed the highest thermal conductivity among all the samples. Therefore, we focus on the thermal conductivity and structural characterization results of the UID, n-type, and n^+ GaN substrates that share a common dopant, Si. Data in Fig. 8 show that the UID and n-type GaN samples exhibit similar crystal quality. Therefore, the lower-thermal conductivity of the n-type GaN sample can be attributed to the larger number density of Si impurities incorporated into the GaN crystal, revealed by the Hall effect (Fig. 9) and SIMS (Table 4) measurement results. On the other hand, the substantially narrower E_2(high) phonon linewidth (Fig. 8(*b*)) of the n^+ sample compared to those for the UID and n-GaN substrates indicates superior crystalline quality. This trend agrees with lower dislocation densities observed in this sample via XRD measurements (Fig. 8(*a*)). While more Si impurities have been incorporated into the n^+ GaN sample (according to the SIMS XRD results in Table 4), its superior crystalline quality significantly reduces the dislocation scattering rate (τ_d^{-1}) in Eq. (6). Due to this reason, the n^+ GaN exhibits the highest thermal conductivity among the three samples sharing a common substitutional dopant, Si.

According to the experimental analysis delineated above, it is observed that GaN samples with similar edge dislocation density exhibit a reduction in their thermal conductivities by the incorporation of substitutional dopants such as Si, Fe, and Mg. For samples sharing a common dopant Si, it was observed that the contribution of phonon-dislocation scattering to the GaN thermal conductivity dominates over phonon-impurity scattering effects.

4 Conclusion

Due to the various doping schemes required to construct ultra-high power vertical GaN electronics, the doping dependence of the GaN thermal conductivity must be understood to build accurate electrothermal models used to design device thermal management solutions. In this study, the thermal conductivity of HVPE-grown bulk GaN substrates employing various doping schemes and concentrations were characterized with a novel SSTR technique. For GaN samples with similar crystal quality, incorporation of substitutional dopants was shown to reduce the thermal conductivity of Fe-doped (92.7 ± 13 W/mK), Mg-doped (152 ± 9.4 W/mK), and Si-doped (86.5 ± 5.0 W/mK) samples as compared to an unintentional doped GaN crystal (193 ± 22 W/mK) with similar crystallinity. However, the highest thermal conductivity among the

investigated specimens was observed in the heaviest Si-doped sample (201 ± 9.4 W/mK) which possessed significantly higher crystalline quality than other GaN samples, confirmed by both XRD and Raman spectroscopy measurements. These results reveal the relative contributions of phonon-dislocation and phonon-impurity scattering effects on the thermal conductivity of bulk GaN crystals and will assist in designing cooling solutions for next-generation vertical GaN power electronic devices.

Acknowledgment

Funding for efforts by the Pennsylvania State University was provided by the AFOSR Young Investigator Program (Grant No. FA9550-17-1-0141, Program Officers: Dr. Brett Pokines and Dr. Michael Kendra, also monitored by Dr. Kenneth Goretta) and the National Science Foundation under Grant No. CBET-1934482.

Funding Data

- Air Force Office of Scientific Research (Funder ID: 10.13039/100000181).
- National Science Foundation (Funder ID: 10.13039/100000001).
- National Science Foundation Division of Chemical, Bioengineering, Environmental, and Transport Systems (Funder ID: 10.13039/100000146).

References

[1] Chatterjee, B., Kim, T. K., Song, Y., Lundh, J. S., Han, S., Shoemaker, D., and Min, J., 2019, "Enhancement of the Electrical and Thermal Performance of AlGaN/GaN HEMTs Using a Novel Resistive Field Plate Structure," 2019 18th IEEE Intersociety Conference on Thermal and Thermomechanical Phenomena in Electronic Systems (ITherm), Las Vegas, NV, May 28–31, pp. 362–369.

[2] Binari, S. C., Klein, P. B., and Kazior, T. E., 2002, "Trapping Effects in GaN and SiC Microwave FETs," Proc. IEEE, **90**(6), pp. 1048–1058.

[3] Daumiller, I., Theron, D., Gaquière, C., Vescan, A., Dietrich, R., Wieszt, A., Leier, H., Vetury, R., Mishra, U. K., Smorchkova, I. P., Keller, S., Nguyen, N. X., Nguyen, C., and Kohn, E., 2001, "Current Instabilities in GaN-Based Devices," IEEE Electron Device Lett., **22**(2), pp. 62–64.

[4] Su, M., Chen, C., Chen, L., Esposto, M., and Rajan, S., 2012, "Challenges in the Automotive Application of GaN Power Switching Devices," International Conference on Compound Semiconductor Manufacturing Technology (CS MANTECH), Boston, MA, Apr. 23–26.

[5] Gupta, C., Chan, S. H., Enatsu, Y., Agarwal, A., Keller, S., and Mishra, U. K., 2016, "OG-FET: An in-Situ Oxide, GaN Interlayer-Based Vertical Trench MOSFET," IEEE Electron Device Lett., **37**(12), pp. 1601–1604.

[6] Ji, D., Li, W., and Chowdhury, S., 2018, "Switching Performance Analysis of GaN OG-FET Using TCAD Device-Circuit-Integrated Model," 2018 IEEE 30th International Symposium on Power Semiconductor Devices and ICs (ISPSD), Chicago, IL, May 13–17, pp. 208–211.

[7] Ji, D., Gupta, C., Chan, S. H., Agarwal, A., Li, W., Keller, S., Mishra, U. K., and Chowdhury, S., 2017, "Demonstrating >1.4 KV OG-FET Performance With a Novel Double Field-Plated Geometry and the Successful Scaling of Large-Area Devices," 2017 IEEE International Electron Devices Meeting (IEDM), San Francisco, CA, Dec. 2–6, pp. 9.4.1–9.4.4.

[8] Oh, S. K., Lundh, J. S., Shervin, S., Chatterjee, B., Lee, D. K., Choi, S., Kwak, J. S., and Ryou, J.-H., 2019, "Thermal Management and Characterization of High-Power Wide-Bandgap Semiconductor Electronic and Photonic Devices in Automotive Applications," ASME J. Electron. Packag., **141**(2), p. 020801.

[9] Lundh, J. S., Song, Y., Chatterjee, B., Baca, A. G., Kaplar, R. J., Armstrong, A. M., Allerman, A. A., Kim, H., and Choi, S., 2019, "Integrated Optical Probing of the Thermal Dynamics of Wide Bandgap," ASME Paper No. IPACK2019-6440.

[10] Mion, C., Muth, J. F., Preble, E. A., and Hanser, D., 2006, "Accurate Dependence of Gallium Nitride Thermal Conductivity on Dislocation Density," Appl. Phys. Lett., **89**(9), p. 092123.

[11] Cahill, D. G., Ford, W. K., Goodson, K. E., Mahan, G. D., Majumdar, A., Maris, H. J., Merlin, R., and Phillpot, S. R., 2003, "Nanoscale Thermal Transport," J. Appl. Phys., **93**(2), pp. 793–818.

[12] Choi, S., Heller, E. R., Dorsey, D., Vetury, R., and Graham, S., 2013, "The Impact of Bias Conditions on Self-Heating in AlGaN/GaN HEMTs," IEEE Trans. Electron Dev., **60**(1), pp. 159–162.

[13] Chatterjee, B., Lundh, J. S., Dallas, J., Kim, H., and Choi, S., 2017, "Electro-Thermal Reliability Study of GaN High Electron Mobility Transistors," 2017 16th IEEE Intersociety Conference on Thermal and Thermomechanical Phenomena in Electronic Systems (ITherm), Orlando, FL, May 30–June 2, pp. 1247–1252.

[14] Wu, Y., Chen, C. Y., and Del Alamo, J. A., 2014, "Activation Energy of Drain-Current Degradation in GaN HEMTs Under High-Power DC Stress," Microelectron. Reliab., **54**(12), pp. 2668–2674.

[15] Coutu, R. A., Lake, R. A., Christiansen, B. D., Heller, E. R., Bozada, C. A., Poling, B. S., Via, G. D., Theimer, J. P., Tetlak, S. E., Vetury, R., and Shealy, J. B., 2016, "Benefits of Considering More Than Temperature Acceleration for GaN HEMT Life Testing," Electronics, **5**(3), p. 32.

[16] Lee, S., Vetury, R., Brown, J. D., Gibb, S. R., Cai, W. Z., Sun, J., Green, D. S., and Shealy, J., 2008, "Reliability Assessment of AlGaN/GaN HEMT Technology on SiC for 48V Applications," 2008 IEEE International Reliability Physics Symposium, Phoenix, AZ, Apr. 27–May 1, pp. 446–449.

[17] Bockowski, M., 2007, "Review: Bulk Growth of Gallium Nitride: Challenges and Difficulties," Cryst. Res. Technol., **1175**(12), pp. 1162–1175.

[18] Iwinska, M., Takekawa, N., Ivanov, V. Y., Amilusik, M., Kruszewski, P., Piotrzkowski, R., Litwin-Staszewska, E., Lucznik, B., Fijalkowski, M., Sochacki, T., Teisseyre, H., Murakami, H., and Bockowski, M., 2017, "Crystal Growth of HVPE-GaN Doped With Germanium," J. Cryst. Growth, **480**, pp. 102–107.

[19] Beechem, T. E., McDonald, A. E., Fuller, E. J., Talin, A. A., Rost, C. M., Maria, J.-P., Gaskins, J. T., Hopkins, P. E., and Allerman, A. A., 2016, "Size Dictated Thermal Conductivity of GaN," J. Appl. Phys., **120**(9), p. 095104.

[20] Palacios, T., Chakraborty, A., Rajan, S., Poblenz, C., Keller, S., DenBaars, S. P., Speck, J. S., and Mishra, U. K., 2005, "High-Power AlGaN/GaN HEMTs for Ka-Band Applications," IEEE Electron Dev. Lett., **26**(11), pp. 781–783.

[21] Rajan, S., Waltereit, P., Poblenz, C., Heikman, S. J., Green, D. S., Speck, J. S., and Mishra, U. K., 2004, "Power Performance of AlGaN-GaN HEMTs Grown on SiC by Plasma-Assisted MBE," IEEE Electron Dev. Lett., **25**(5), pp. 247–249.

[22] Look, D. C., and Sizelove, J. R., 1999, "Dislocation Scattering in GaN," Phys. Rev. Lett., **82**(6), pp. 1237–1240.

[23] Simpkins, B. S., Yu, E. T., Waltereit, P., and Speck, J. S., 2003, "Correlated Scanning Kelvin Probe and Conductive Atomic Force Microscopy Studies of Dislocations in Gallium Nitride," J. Appl. Phys., **94**(3), pp. 1448–1453.

[24] Hsu, J. W. P., Manfra, M. J., Molnar, R. J., Heying, B., and Speck, J. S., 2002, "Direct Imaging of Reverse-Bias Leakage Through Pure Screw Dislocations in GaN Films Grown by Molecular Beam Epitaxy on GaN Templates," Appl. Phys. Lett., **81**(1), pp. 79–81.

[25] Zou, J., Kotchetkov, D., Balandin, A. A., Florescu, D. I., and Pollak, F. H., 2002, "Thermal Conductivity of GaN Films: Effects of Impurities and Dislocations," J. Appl. Phys., **92**(5), pp. 2534–2539.

[26] Jeżowski, A., Stachowiak, P., Plackowski, T., Suski, T., Krukowski, S., Boćkowski, M., Grzegory, I., Danilchenko, B., and Paszkiewicz, T., 2003, "Thermal Conductivity of GaN Crystals Grown by High Pressure Method," Phys. Status Solidi, **240**(2), pp. 447–450.

[27] Kotchetkov, D., Zou, J., Balandin, A. A., Florescu, D. I., and Pollak, F. H., 2001, "Effect of Dislocations on Thermal Conductivity of GaN Layers," Appl. Phys. Lett., **79**(26), pp. 4316–4318.

[28] Kizilyalli, I. C., Edwards, A. P., Aktas, O., Prunty, T., and Bour, D., 2015, "Vertical Power P-n Diodes Based on Bulk GaN," IEEE Trans. Electron Dev., **62**(2), pp. 414–422.

[29] Witek, A., 1998, "Some Aspects of Thermal Conductivity of Isotopically Pure Diamond—A Comparison With Nitrides," Diam. Relat. Mater., **7**(7), pp. 962–964.

[30] Kamatagi, M. D., Sankeshwar, N. S., and Mulimani, B. G., 2007, "Thermal Conductivity of GaN," Diam. Relat. Mater., **16**(1), pp. 98–106.

[31] Ziade, E., Yang, J., Brummer, G., Nothern, D., Moustakas, T., and Schmidt, A. J., 2017, "Thickness Dependent Thermal Conductivity of Gallium Nitride," Appl. Phys. Lett., **110**(3), p. 031903.

[32] Bougher, T. L., Yates, L., Lo, C.-F., Johnson, W., Graham, S., and Cola, B. A., 2016, "Thermal Boundary Resistance in GaN Films Measured by Time Domain Thermoreflectance With Robust Monte Carlo Uncertainty Estimation," Nanoscale Microscale Thermophys. Eng., **20**(1), pp. 22–32.

[33] Chatterjee, B., Dundar, C., Beechem, T. E., Heller, E., Kendig, D., Kim, H., Donmezer, N., and Choi, S., 2020, "Nanoscale Electro-Thermal Interactions in AlGaN/GaN High Electron Mobility Transistors," J. Appl. Phys., **127**(4), p. 44502.

[34] Rounds, R., Sarkar, B., Sochacki, T., Bockowski, M., Imanishi, M., Mori, Y., Kirste, R., Collazo, R., Sitar, Z., and Phys, J. A., 2018, "Thermal Conductivity of GaN Single Crystals: Influence of Impurities Incorporated in Different Growth Processes," J. Appl. Phys., **124**(10), p. 105106.

[35] Cho, J., Li, Y., Hoke, W. E., Altman, D. H., Asheghi, M., and Goodson, K. E., 2014, "Phonon Scattering in Strained Transition Layers for GaN Heteroepitaxy," Phys. Rev. B., **115301**, pp. 1–11.

[36] Ziade, E., Yang, J., Brummer, G., and Nothern, D., 2017, "Thermal Transport Through GaN – SiC Interfaces From 300 to 600 K," Appl. Phys. Lett., **091605**, pp. 1–5.

[37] Luo, C.-Y., Marchand, H., Clarke, D. R., and DenBaars, S. P., 1999, "Thermal Conductivity of Lateral Epitaxial Overgrown GaN Films," Appl. Phys. Lett., **75**(26), pp. 4151–4153.

[38] Braun, J. L., Olson, D. H., Gaskins, J. T., and Hopkins, P. E., 2019, "A Steady-State Thermoreflectance Method to Measure Thermal Conductivity," Rev. Sci. Instrum., **90**(2), p. 24905.

[39] Schmidt, A. J., Cheaito, R., and Chiesa, M., 2009, "A Frequency-Domain Thermoreflectance Method for the Characterization of Thermal Properties," Rev. Sci. Instrum., **80**(9), p. 094901.

[40] Cahill, D. G., 2004, "Analysis of Heat Flow in Layered Structures for Time-Domain Thermoreflectance," Rev. Sci. Instrum., **75**(12), pp. 5119–5122.

[41] Fujikura, H., Konno, T., Yoshida, T., and Horikiri, F., 2017, "Hydride-Vapor-Phase Epitaxial Growth of Highly Pure GaN Layers With Smooth as-Grown Surfaces on Freestanding GaN Substrates," Jpn. J. Appl. Phys., **56**(8), p. 085503.
[42] Fleischmann, S., Richter, E., Mogilatenko, A., Weyers, M., and Tränkle, G., 2019, "Influence of Quartz on Silicon Incorporation in HVPE Grown AlN," J. Cryst. Growth, **507**, pp. 295–298.
[43] Braun, J. L., Szwejkowski, C. J., Giri, A., and Hopkins, P. E., 2018, "On the Steady-State Temperature Rise During Laser Heating of Multilayer Thin Films in Optical Pump–Probe Techniques," ASME J. Heat Transfer, **140**(5), p. 052801.
[44] Kaganer, V. M., Brandt, O., Trampert, A., and Ploog, K. H., 2005, "X-Ray Diffraction Peak Profiles From Threading Dislocations in GaN Epitaxial Films," Phys. Rev. B, **72**(4), p. 45423.
[45] Heinke, H., Kirchner, V., Einfeldt, S., and Hommel, D., 1999, "Analysis of the Defect Structure of Epitaxial GaN," Phys. Status Solidi, **176**(1), pp. 391–395.
[46] Metzger, T., Höpler, R., Born, E., Ambacher, O., Stutzmann, M., Stömmer, R., Schuster, M., Göbel, H., Christiansen, S., Albrecht, M., and Strunk, H. P., 1998, "Defect Structure of Epitaxial GaN Films Determined by Transmission Electron Microscopy and Triple-Axis X-Ray Diffractometry," Philos. Mag. A, **77**(4), pp. 1013–1025.
[47] Chierchia, R., Böttcher, T., Heinke, H., Einfeldt, S., Figge, S., and Hommel, D., 2003, "Microstructure of Heteroepitaxial GaN Revealed by X-Ray Diffraction," J. Appl. Phys., **93**(11), pp. 8918–8925.
[48] Heinke, H., Kirchner, V., Einfeldt, S., and Hommel, D., 2000, "X-Ray Diffraction Analysis of the Defect Structure in Epitaxial GaN," Appl. Phys. Lett., **77**(14), pp. 2145–2147.
[49] Srikant, V., Speck, J. S., and Clarke, D. R., 1997, "Mosaic Structure in Epitaxial Thin Films Having Large Lattice Mismatch," J. Appl. Phys., **82**(9), pp. 4286–4295.
[50] Amano, H., Takeuchi, T., Sakai, H., Yamaguchi, S., Wetzel, C., and Akasaki, I., 1998, "Heteroepitaxy of Group III Nitrides for Device Applications," Mater. Sci. Forum, **264–268**, pp. 1115–1120.
[51] Kuball, M., and Pomeroy, J. W., 2016, "A Review of Raman Thermography for Electronic and Opto-Electronic Device Measurement With Submicron Spatial and Nanosecond Temporal Resolution," IEEE Trans. Device Mater. Reliab., **16**(4), pp. 667–684.
[52] Bergman, L., and Nemanich, R. J., 1996, "Raman Spectroscopy for Characterization of Hard, Wide-Bandgap Semiconductors: Diamond, GaN, GaAlN, AlN, BN," Annu. Rev. Mater. Sci., **26**(1), pp. 551–579.
[53] Choi, S., Heller, E. R., Dorsey, D., Vetury, R., and Graham, S., 2013, "Thermometry of AlGaN/GaN HEMTs Using Multispectral Raman Features," IEEE Trans. Electron Devices, **60**(6), pp. 1898–1904.
[54] Choi, S., Heller, E., Dorsey, D., Vetury, R., and Graham, S., 2013, "Analysis of the Residual Stress Distribution in AlGaN/GaN High Electron Mobility Transistors," J. Appl. Phys., **113**(9), p. 093510.
[55] Kuball, M., 2001, "Raman Spectroscopy of GaN, AlGaN and AlN for Process and Growth Monitoring/Control," Surf. Interface Anal., **31**(10), pp. 987–999.
[56] Beechem, T., Christensen, A., Graham, S., and Green, D., 2008, "Micro-Raman Thermometry in the Presence of Complex Stresses in GaN Devices," J. Appl. Phys., **103**(12), p. 124501.
[57] Ponce, F. A., Steeds, J. W., Dyer, C. D., and Pitt, G. D., 1996, "Direct Imaging of Impurity-Induced Raman Scattering in GaN," Appl. Phys. Lett., **69**(18), pp. 2650–2652.
[58] Huang, Y., Chen, X. D., Fung, S., Beling, C. D., Ling, C. C., Wei, Z. F., Xu, S. J., and Zhi, C. Y., 2004, "The Depth-Profiled Carrier Concentration and Scattering Mechanism in Undoped GaN Film Grown on Sapphire," J. Appl. Phys., **96**(2), pp. 1120–1126.
[59] Özgür, Ü., Gu, X., Chevtchenko, S., Spradlin, J., Cho, S. J., Morkoç, H., Pollak, F. H., Everitt, H. O., Nemeth, B., and Nause, J. E., 2006, "Thermal Conductivity of Bulk ZnO After Different Thermal Treatments," J. Electron. Mater., **35**(4), pp. 550–555.
[60] Nagai, H., Zhu, Q. S., Kawaguchi, Y., Hiramatsu, K., and Sawaki, N., 1998, "Hole Trap Levels in Mg-Doped GaN Grown by Metalorganic Vapor Phase Epitaxy," Appl. Phys. Lett., **73**(14), pp. 2024–2026.
[61] Kozodoy, P., Xing, H., DenBaars, S. P., Mishra, U. K., Saxler, A., Perrin, R., Elhamri, S., and Mitchel, W. C., 2000, "Heavy Doping Effects in Mg-Doped GaN," J. Appl. Phys., **87**(4), pp. 1832–1835.
[62] Simon, R. B., Anaya, J., and Kuball, M., 2014, "Thermal Conductivity of Bulk GaN—Effects of Oxygen, Magnesium Doping, and Strain Field Compensation," **105**(20), pp. 202105–202115.
[63] Van de Walle, C. G., 2003, "Effects of Impurities on the Lattice Parameters of GaN," Phys. Rev. B, **68**(16), pp. 1–5.
[64] Xu, R. L., Muñoz Rojo, M., Islam, S. M., Sood, A., Vareskic, B., Katre, A., Mingo, N., Goodson, K. E., Xing, H. G., Jena, D., and Pop, E., 2019, "Thermal Conductivity of Crystalline AlN and the Influence of Atomic-Scale Defects," J. Appl. Phys., **126**(18), p. 185105.